Influences of iron and manganese cycling on alkalinity in the redox stratified water column of Chesapeake Bay

Aubin Thibault de Chanvalon[1,2], George W. Luther[2], Emily R. Estes[2], Jennifer Necker[2], Bradley M. Tebo[3], Jianzhong Su[4,5], Wei-Jun Cai[4]

[1]Université de Pau et des Pays de l'Adour, E2S UPPA, CNRS, IPREM, Pau, France.
[2]School of Marine Science and Policy, University of Delaware, Lewes, Delaware, 19958 USA
[3]Division of Environmental and Biomolecular Systems, 3181 SW Sam Jackson Park Road, Portland, OR 97239, USA; Current address: Department of Chemistry, University of Washington, Seattle,WA 98195-1700
[4]School of Marine Science and Policy, University of Delaware, Newark, Delaware, USA
[5]State Key Laboratory of Marine Resources Utilization in South China Sea, Hainan University, Haikou, China

Correspondence to: A. Thibault de Chanvalon (aubin.thibault-de-chanvalon@univ-pau.fr)

Abstract. The coastal alkalinity cycle controls the global burial of carbonate which modulates the ability of the ocean to trap anthropogenic CO_2. Twelve high vertical resolution profiles from the temperate Chesapeake Bay estuary during two summers allow precise description of carbonate dynamics over the salinity and redox gradient along with the measurement of the speciation of most redox sensitive elements. In the presence of oxygen, carbonate dissolution, primary production and aerobic respiration are able to explain the evolution of total alkalinity (TA) versus dissolved inorganic carbon (DIC), once corrected for fresh and oceanic water mixing. A significant flooding event in 2018 prevented the trapping of atmospheric CO_2 in the estuary and favoured carbonate dissolution to balance DIC consumption from photosynthesis. In oxygen depleted waters, a particularly high ratio of alkalinity versus DIC occurred ($\Delta TAex/\Delta DICex = 2.4$), that has not been previously reported in the literature, and that seemed invariant over the two years. The stoichiometric analysis agrees with Mn measurements to explain this carbonate signature by the critical role of MnO_2 reduction followed by Mn carbonate precipitation. Our results underline that Fe and Mn are critical elements of the alkalinity cycle, especially due to their ability to limit the H_2S oxidation into SO_4^{2-} and by favouring sulphur burial.

1 Introduction

About a third of anthropogenic CO_2 emission is rapidly trapped by dissolution in the ocean as dissolved inorganic carbon (DIC) which is dominated by bicarbonate ions (HCO_3^-, Friedlingstein et al., 2019). At the century time scale, atmosphere-ocean exchanges result in oceanic HCO_3^- enrichment not associated with a Ca^{2+} enrichment, in contrast to the HCO_3^- released from continental erosion (preponderant at thousands to a million year scale, Urey, 1952). This disequilibrium corresponds to an excess of proton release compared to carbonate ions during CO_2 dissolution that is only balanced in the deep ocean by increasing Ca^{2+} production from carbonate dissolution, a process named the chemical carbonate compensation (Boudreau et al., 2018). However, in most shallow water, where carbonate precipitation largely predominates over dissolution and accounts for 2/3 of buried carbonate (Smith and Mackenzie, 2016), other, localised processes may constrain the carbonate dynamic (Borges et al., 2006; Lohrenz et al., 2010). For example, some calcifying species may slow down their carbonate precipitation in case of pH decrease (so called biological carbonate compensation; Boudreau et al., 2018). As another example, in estuaries, the seasonality of river flow, temperature and continental erosion modulate $CaCO_3$ dissolution (e.g. Su et al., 2020b), atmospheric CO_2 exchanges (e.g. Borges et al., 2018) or respiratory activity (Abril et al., 2003). As recently highlighted (Middelburg et al., 2020), the transfer of carbonate particles over estuaries is poorly estimated due to a sparse dataset (Meybeck, 1987).

To better constrain the carbonate cycle in temperate microtidal estuaries and the associated HCO_3^- dynamics, we sampled a stratified water column in the Chesapeake Bay a dozen times over two campaigns with a high vertical resolution (down to 10 cm). This protocol allows a precise description of carbonate dynamics over a redox gradient along with the measurement of the speciation of most redox sensitive elements. Such sampling can thus illustrate carbonate chemistry on transitioning from oxygenated waters to waters devoid of oxygen as usually only encountered in sediments or in anoxic lakes or seas (*e.g.* Black Sea). The original observed changes of alkalinity versus DIC changes are interpreted based on anoxic reactions occurring along the redox gradient.

2 Materials and methods

2.1 Sampling

During two sampling campaign from August 3rd to 9th, 2017 and July 28th to August 3rd 2018 eleven profile casts were conducted in a 25 m water depth in the Chesapeake Bay (Station 858, 38°58.54'N; 076°22.22'W). The Susquehanna River is the main tributary of the bay representing on average 2/3 of the fresh water input (Zhang et al., 2015). Despite similar season, the two campaigns occurred at very different river flow with about 850 m^3 s^{-1} in 2017 versus 8500 m^3 s^{-1} in 2018 due to release of flood waters from the Conowingo Dam and which corresponds to flooding which occurs on average every 3.5 years (return period of 3.5 years ,USGS survey).

Each CTD cast was performed during low or high tide slack periods. An oxygen sensor (Clark electrode, SBE Inc.;
55 detection limit of 1 μM) and fluorescence sensor (Eco-FL Fluorometer, WETLabs) were part of the CTD Rosette to take measurements during sampling. Also, a submersible all plastic pump profiler was attached with the pump near the sensor orifices allowing measurement and sampling at a resolution of a few centimetres over 25 m water depth. Water was pumped to the deck within 1 minute and water passed through a flow through voltammetry system measuring continuously O_2, Mn(II), Fe(II), organically complexed Fe(III), FeS clusters, H_2S and polysulfides (Hudson et al., 2019). When redox interfaces were
60 identified, samples were filtered through an acetate cartridge filter (pore size 0.45 μm) for pH and inorganic carbon parameters, which were processed onboard within a few hours after sampling in order to conserve chemical speciation. The pump profiler system was cleaned with DI water onboard the deck of the ship after deployment. No coating effects were observed with the pump system.

2.2 Discrete Measurements

65 For each sample, all redox species were determined in the through flow voltammetry system using cyclic voltammetry with a 100 μm Au/ Hg amalgam PEEK microelectrode prepared according to Luther et al. (2008) connected to a DLK-60 electrochemical analyser from Analytical Instrument Systems Inc. The detection limit of this method is 0.2 μM for sulfide and polysulfides. Discrete samples for the determination of NO_2^-, Fe and Mn species were filtered through nylon luer-lock syringe filters (Millipore, 0.20 μm) filters. Iron was measured based on the ferrozine method (Stookey, 1970): after HCl acidification
70 and an optional reduction step with hydroxylamine hydrochloric (final concentration 0.7 M) for 1 hour, ammonium actetate (final concentration 0.5 M) and ferrozine (final concentration 1 mM) were added and absorbance at 562 nm was read with a diode array spectrophotometer (Hewlett Packard 8452B). Limit of detection is 100 nM for Fe(II). Shipboard nitrite determination was performed using the method of Grasshoff (1983). To 25 ml of sample, 0.5 ml of 58mM sulfanilamide in 10% v/v HCl and 0.5 ml of a 4mM N(1-naphthyl)ethylene diamine hydrochloride solution were added. Samples with added
75 reagents were shaken and left to sit for 15 min, followed by UV–Vis analysis at 540 nm using a 10-cm cell to increase detection limits. Calibration curves were constructed using sodium nitrite. Limit of detection is 10 nM for NO_2^-.

Dissolved manganese was determined by displacement of a Cd(II)-porphyrin complex with Mn(II) to form the Mn(II)-porphyrin complex (Ishii et al., 1982). Mn(III) species were identified based on slower reactivity with the Cd complex (Madison et al., 2011) as modified in Thibault de Chanvalon and Luther (2019). Alternatively, Mn(III) species were identified
80 after HCl treatment (down to pH=1.5) follow by filtration in order to flocculate and eliminate the dissolved manganese bound to humic material by filtration (Oldham et al., 2017b). Limit of detection is 50 nM for Mn(II). MnOx was measured on 20 mL samples of suspended material retained on 0.2 μm filters by the Leucoberbelin blue (LBB) method (Jones et al., 2019). Four millilitres of a reagent solution ([LBB]= 78 μM, [acetic acid]=14mM) react with the filter and the absorbance is read at 624 nm. $KMnO_4$ was used to calibrate the LBB method which allows the calculation the electron equivalents obtained from
85 particulate MnOx. Results are given in as MnO_2 equivalent with a limit of detection of 0.1 μM and an uncertainty below 5%.

The DIC samples were preserved in 250-mL borosilicate glass bottle with 50 μL saturated $HgCl_2$ solution. The TA samples were not poisoned to prevent HgS precipitation and H+ release in anoxic and low salinity waters (Cai et al. 2017). The DIC samples were measured by a nondispersive infrared analyzer (AS-C3, Apollo Scitech) within a week (Huang et al. 2012). The total alkalinity (TA) was analyzed by Gran titration in an open-cell setting (AS-ALK2, Apollo Scitech) inboard within 24 h of

90   collection (Cai et al. 2010a). The precision for DIC and TA was about 0.1‰. Both DIC and TA measurements were calibrated against certified reference materials. The pH samples were measured onboard at 25 ° C within 1 h of collection using an Orion Ross glass electrode, and calibrated with NIST standard buffers. The pCO2, calcite saturation were calculated from measured DIC and TA via an excel sheet implemented with values from (Millero, 1995) and further validated using CO2sys program. The measured TA was found highly correlated to TA calculated with CO2sys using pH and DIC as input value (r^2 = 0.998,

95   slope = 1.03) suggesting low effect of organic alkalinity (Cotovicz Jr. et al., 2016).

2.3 Models of biogeochemical process on TA and DIC

2.3.1 Observed changes induced by biogeochemical process

To distinguish TA and DIC changes produced by biogeochemical processes from the river/ocean mixing, the excess of TA and DIC, noted TAex and DICex have to be calculated. This excess corresponds to the cumulative effects from all unknown

100   biogeochemical processes observed. As total concentrations, TA and DIC are conservative during mixing and can be easily calculated as the deviation from the river-ocean mixing line after identification of riverine and oceanic endmembers. In contrast, pH and the concentrations of individual C species are not conservative. The oceanic endmember selected in this study was the one proposed by Su et al. (2020a) for both DIC and TA. However, the upstream estuary endmember from Su et al. (2020a) corresponded to the Chesapeake Bay in 2016 with a river flow of only 226 m^3 s^{-1}. The two campaigns described here

105   are characterised by much higher river flow. Since large variations exist in the upstream estuary endmember mainly due to changes of weathering intensity and riverine discharge (Meybeck, 2003; Joesoef et al., 2017), we slightly modify the TA endmember of Su et al. (2020a) to improve the fit with in situ measurements with the lowest measured salinity (Fig. A1). Such changes were not necessary for DICex calculation. This endmember is not a river endmember (Su et al., 2020a) but correspond to a salinity above 1.5 preventing any interpretation for biological activity in the fresh water part of the estuary (Meybeck et

110   al., 1988). Compared to Su et al. (2020a), the slope change associated is mostly insignificant (TAex/DICex differs by less than 0.2) and represents the uncertainty of our description. The TAex and DICex correspond to an excess from a sum of reactions spread all over the estuary and can therefore decomposed into several components induced by multiple localised geochemical reactions, ΔTAex and ΔDICex.

2.3.2 TA changes indicated by reactions' stoichiometry

115   The simplest way to calculate the TA changes induced by individual, localised, geochemical reactions (ΔTAex) is to do a direct look to reaction stoichiometry. Indeed, it is possible to mathematically separate acid active and acid inactive species.

Active species are defined as species forming acid-base couples whose one form is able to exchange protons during the titration of a sample down to pH 4.5 either as electron donor or as acceptor, such as NH_3 or HCO_3^- while inactive species include Cl^-, SO_4^{2-} and Ca^{2+} among others. Writing z, the charge held by a species, the electroneutrality of water can be written as Eq. (1),

$$0 = \sum z_{inactive} + \sum z_{active} \tag{1}$$

120   The total alkalinity (TA) corresponds to the quantity of acid added to titrate a solution down to pH 4.5 (Dickson, 1981), according to Eq. (2), with the example of HCl as acid and B^- any titrated base.

$$HCl + B^- \rightarrow BH + Cl^- \tag{2}$$

Assuming a complete reaction, the quantity of acid added is equal to the negative charges consumed from the active species pool (Cl^- is inactive). Indeed, the titration transfers the charges from the acid active pool to the acid inactive pool. Thus, the total alkalinity corresponds to the loss of negative charges (or gain of positive charges) for active species produced by the pH

125   change from the initial pH = pHini to pH = 4.5 (Eq. (3)):

$$TA = \sum z_{active}^{pH=4.5} - \sum z_{active}^{pHini} \tag{3}$$

Equation (1) can be reorganized and combined with Eq. (3) leading to Eq. (4) :

$$\sum z_{inactive} = -\sum z_{active}^{pHini} + \sum z_{active}^{pH=4.5} - \sum z_{active}^{pH=4.5}$$

$$TA = \sum z_{inactive} + \sum z_{active}^{pH=4.5} \tag{4}$$

From Eq. (4), one can easily deduce the changes of alkalinity. Most of the time, the only charged active species at pH = 4.5, are $H_2PO_4^-$ and NH_4^+. In that respect, whatever the initial pH and the acid-base equilibrium of species in the sample, the sum of phosphate species will count negatively and the sum of ammonium species will count positively. Strictly speaking, at

130   pH=4.5, acid species with pKa between 2.5 and 6.5, such as F^- and NO_2^-, would be only partially titrated and the charge equals their concentration multiplied by a correction factor of $(1+10^{pKa-4.5})^{-1}$, but this correction can be neglected to a first approximation. The Eq. (4) corresponds to those published in Soetaert et al. (2007) or Wolf-Gladrow et al. (2007) whose equation 32 can be find back replacing the two term in Eq. (4) by:

$$\sum z_{inactive} = [Na^+] + 2\,[Mg^{2+}] + 2\,[Ca^{2+}] + [K^+] + 2[Sr^{2+}] + \cdots - [Cl^-] - [Br^-]$$
$$- [NO_3^-] - 2TSO4 - THF - THNO2 - \cdots$$

$$\sum z_{active}^{pH=4.5} = -TPO4 + TNH3$$

135 where TPO4 = $[H_3PO_4]$ + $[H_2PO_4^-]$ + $[HPO_4^{2-}]$ + $[PO_4^{3-}]$, TNH3 = $[NH_3]$ + $[NH_4^+]$, TSO4 = $[SO_4^{2-}]$ + $[HSO_4^-]$, THF = $[F^-]$ + $[HF]$, and THNO2 = $[NO_2^-]$ + $[HNO_2]$. However, the Eq. (4) is more synthetic and more general. For example, in suboxic water, specific species such as polysulfides (as HS_8^{2-}, Rickard and Luther, 2007) and in highly productive environment, carboxylic group from DOC can be easily added as soon as the bearing charges at pH = 4.5 are known. Finally, note that the definition of active species used differs from the weak acid-base couple definition, since our definition classifies the weak acid –based couples with pKa between -1.75 and 4.5 as inactive species, but the reasoning would be similar if the term

140 active/inactive species is changed by weak/strong acid-base couple.

2.3.3 Linear combinations of reactions

To estimate the participation of each reaction to the observed changes of TAex, DICex and AOU or H_2S, a linear combination of pre-selected reactions is calculated. This combination has to fit 3 equations (one for each parameter) which allows a maximum of 3 variables to be used to solve the system. Each reaction being one variable, a limited number of reactions

145 is selected as candidates based on the discussion (see section 3.3.2). Then, the system is solved with the minimum possible reactions.

3 Results and Discussion

3.1 Water column stratification

High-resolution (< 1 m) profiles of carbonate and redox chemistry are plotted against salinity in Fig. 1. These data result

150 from the 11 CTD casts performed over 1 week during each campaign and correspond to depths ranging from 2 to 25 meters. While direct plots against depth generate noisy profiles that are less informative, plots against salinity provide consistent information about the processes. Despite the overall much lower salinity due to a near 7-fold flow increase in 2018 than 2017 (5800 m s^{-1} in 2018 versus 850 m^3 s^{-1} in 2017), similar zonation of the water column occurred. A surface layer (named primary production zone or PP in Fig. 1) is characterized by high amount of O_2 (about or above 100% saturation), high pH (above 7.5),

155 high day to day temperature variation (above 1 °C between different days) and low pCO_2 (below atmospheric CO_2 of 400 µatm). This signature corresponds to important atmospheric exchange and primary production (PP). Fluorescence (not shown) correlates with pH as expected for primary production (pH = Fluo (mV) x 13 +7.14, r^2=0.8 in 2017 and r^2=0.9 in 2018). Below, with increasing depth, an important increase of pCO_2 accompanying the decrease of O_2, pH and temperature is visible. A relatively invariable low O_2 zone (called ILO in Fig. 1) is here defined by the depth invariance of O_2 concentrations, and

160 corresponds to a concentration of about 30 µM in 2017 and 110 µM in 2018. Other species are also relatively stable for this depth such as pCO_2, at about 2500 µatm in 2017 and 1800 µatm in 2018, and pH, about 7.3 in 2017 and 7.4 in 2018. Deeper, where the oxygen is not detectable (< ~ 1 µM), the so-called suboxic zone corresponds to a pH minimum at 7.2 that generates a pCO_2 maximum. The deepest layer is a sulfidic layer in which the pH seems quite stable at 7.4 and 7.3 in 2017 and 2018 respectively. The main changes between the two campaigns correspond to a greater oxygen penetration in 2018, preventing

165   nitrite accumulation, and to the appearance of a surface layer (with salinity below 3) that stands above the primary production

zone in 2018.
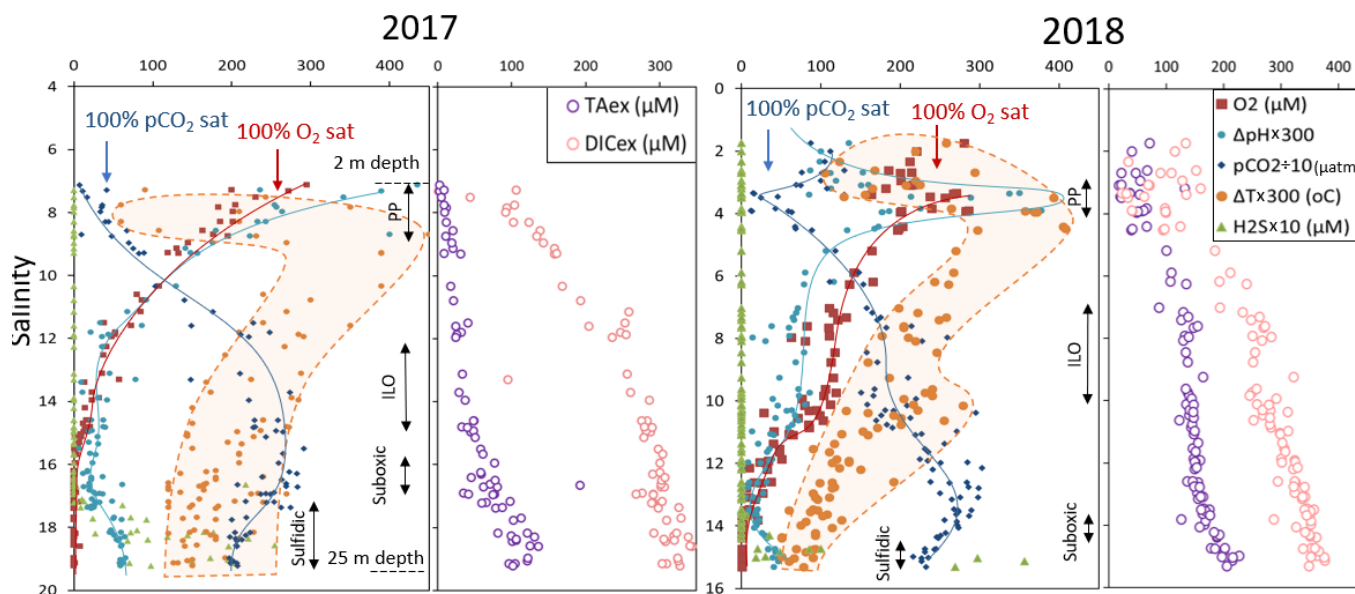
Figure 1: Superimposed carbonate and redox chemistry profiles over 11 casts. Simple mathematic transformation allows to plot all variable on the same scale, lines are only here to guide eyes. Base line for temperature is 25 °C and base line for pH 7.175. For example, pH maximum value of 400 correspond to a pH=400/300+7.175=8.5, a reading at 100 for pCO₂÷10 indicates a value of pCO₂ = 1000 µatm.

The development of the suboxic zone during summer (Su et al., 2021) and the regularity of this development over the years (Sholkovitz et al., 1992; Trouwborst et al., 2006; Lewis et al., 2007; Cai et al., 2017; Oldham et al., 2017a), requires the presence of species able to rapidly oxidise the H_2S mixing upward and to reduce the O_2 mixing downward. The three main

170   redox couples known to play this role, NO_3^- / NO_2^-, MnO_x / Mn^{2+} and Fe^{3+} / Fe^{2+} are described in the Fig. 2 by the superimposition of all cast results against salinity. Four representative casts are plotted in the Fig. A2. NO_2^- reaches a maximum in the ILO zone, at low but measurable oxygen concentrations. Because of the presence of oxygen, the NO_2^- production would be more likely associated with nitrification of the NH_4^+ diffusing upward rather than denitrification despite the possibility of reducing conditions occurrence in micro niches. Just below oxygen depletion, in the suboxic zone, MnOx reaches a maximum

175   probably produced by the Mn^{2+} diffusing upward that is biologically oxidized by very low, undetected, O_2 concentration (Clement et al., 2009). Additionally, Mn^{2+} could be oxidized by the nitrite diffusing downward (thermodynamically favourable (Luther, 2010)), it is also possible that the Mn oxidation is produced by chemodenitrification *i.e.* by reduction of (not measured) nitrate into nitrite. The MnOx decrease fits perfectly to the Mn^{2+} increases in sulfidic conditions (Fig. 2) according to the reduction of settling MnOx by H_2S. The increase of total manganese concentration with depth may result from sedimentary

180   efflux or dissolved manganese trapping in more stagnant bottom water. No Mn(III) was detected with the porphyrin kinetics method (Thibault de Chanvalon and Luther, 2019) but about 30% of the total dissolved manganese flocculated after

acidification down to pH 1.5 when analysed in 2017. Although similar recycling is expected for iron, fresh precipitates are harder to catch due to higher particles content, and, in our study, lower dissolved total Fe concentration. Some features are discernible for a single cast (Fig. A2), but overall the only merging picture is an increase with proximity to the sediment
185 interface for dissolved Fe(III) and Fe(II) and solid Fe(III) and Fe(II) (Fig. 2).
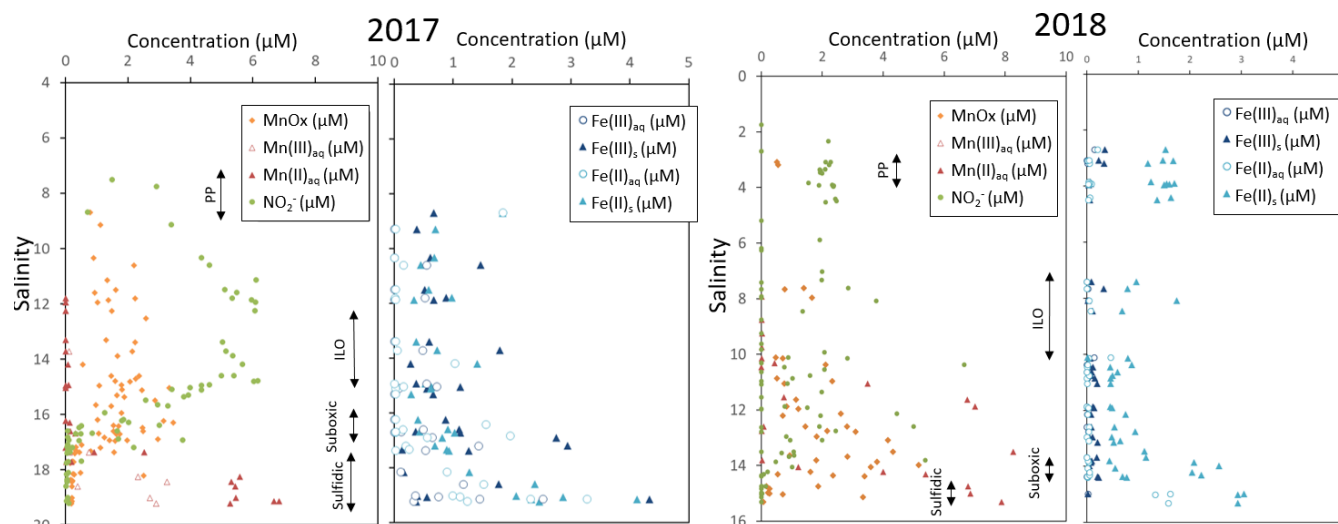
Figure 2: Mn, Fe and nitrate profiles build by superimposition of 11 casts for each campaign.

3.2 River flow control

In rivers, the carbonate system equilibria depend on processes as varied as weathering intensity, draining bedrock and *in situ* biological activities. The inspection of dissolved inorganic carbon (DIC) changes versus total alkalinity (TA) changes is a frequent and efficient method to unravel the origin of these changes whereas other related parameters such as pCO_2 or pH are
190 non-conservative during mixing and harder to interpret (*e.g.* Cai et al. 2017). However, due to river mixing with ocean waters, both TA and DIC change with salinity (S) as observed in the Chesapeake Bay during our campaigns (r^2>0.95, Fig. A1). The calculation of the excess of TA and DIC, named TAex and DICex (see section 2.3.1), is required to interpret further biogeochemical processes (Su et al., 2020b).

DICex increases progressively with depth up to about 330 µM and 350 µM at 25 m depth in 2017 and 2018 respectively
195 (Fig. 1). The plot of TAex versus DICex (Fig. 3a) shows at the lowest observed salinity (7.1 in 2017 and 1.7 in 2018), an intercept for TAex = 0 corresponding to DICex ~ 40 µM. This offset is within the uncertainty of the endmember calculation even if slight DICex background enrichment has been modelled (Shen et al., 2019) resulting from faster atmospheric equilibration of O_2 than CO_2 after respiration reactions. Interestingly, the relative changes of DICex and TAex, further named ΔTAex and ΔDICex, does not depend on the endmember calculation and their ratio presents much lower uncertainties (about
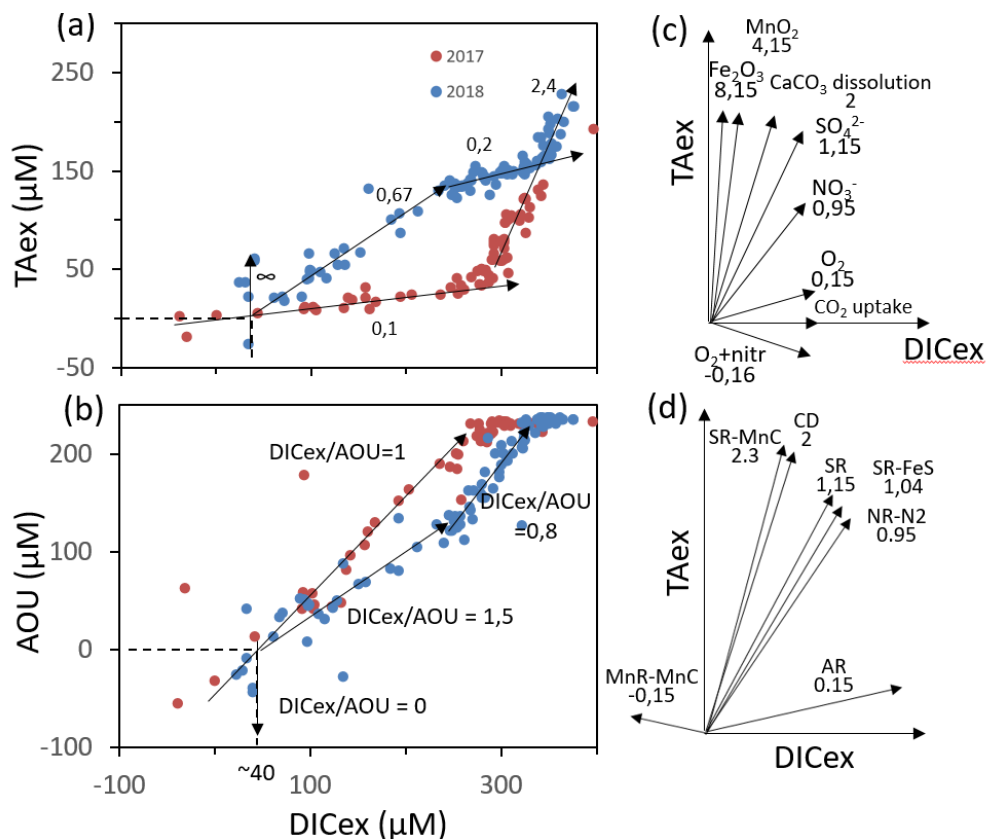
Figure 3: Description of the Taex/DICex/AOU system. (a) and (b) panels show samples measured along with interpretative slope discussed in the main text. Panels (c) and (d) show theoretical slope of Taex/DICex, (c) from seven primary redox reaction in seawater (pH=8,2) described in Soetaert et al. (2007). (d) from combination of reaction discussed in the main text.

200   0.1) facilitating their interpretation. In 2017, TAex stayed almost constant up to the oxic zone (Fig. 3a) with a ΔTAex/ΔDICex

ratio of 0.1 ± 0.1 which indicates a net aerobic respiration (AR) (theoretical slope of ΔTAex/ΔDICex = 0.15 see Table 1 and

Fig. 3c). The AOU increase (Fig. 3b) confirms this possibility with a ΔDICex/ΔAOU signal similar to the expected theoretical

slope of 1 for AR (Table 1). Note that this ΔTAex/ΔDICex/ΔAOU signature stands for absent or negligible nitrification

following respiration. In case of nitrification, the theoretical slopes should be ΔTAex/ΔDICex = - 0.165 and ΔDICex/ΔAOU

205   = 0.76 as proposed by Zeebe and Wolf-Gladrow (2001). The absence of noticeable nitrification can be explain by slow kinetics

of NH_4^+ oxidation, with a half-life time estimated between a few days in estuaries (Horrigan et al., 1990) to multiple years in

coastal environments (Heiss and Fulweiler, 2016). As a comparison, other NH_4^+ fates, such as adsorption leads to ammonium

half life time of about a few minutes (Alshameri et al., 2018) to a few hours (Raaphorst and Malschaert, 1996) depending on

the concentration of fine particles. Additionally, algae are known to use NH_4^+ as a N source (Raven et al., 1992) and NH_4^+ can

210   be directly assimilated by heterotrophic organisms. Finally, for 2017, despite pCO_2 being below atmospheric saturation at

about 2 m depth (Fig. 1), the possible CO_2 invasion does not significantly modify the observed $\Delta DICex/\Delta AOU$ signal at the shallowest depth sampled.

In 2018, this surface water history did not repeat as fresh and light water masses brought by the exceptional flood drastically
215 modified the carbonate system equilibrium. First, a low salinity layer with pCO_2 at 1000 µatm overlays the primary production layer (Fig. 1), preventing the uptake of atmospheric CO_2 by primary production as was observed for other years (Chen et al., 2020). Just below the air-sea interface, the lock down of atmospheric exchanges by the law salinity layer produces supersaturation of trapped O_2 (Fig. 1, for S between 3 and 4). In Fig. 3a and 3b, this process translates into a vertical distribution at DICex = 40 µM associated with negative AOU and slightly positive TAex. This original signature can be modelled by the
220 combination of simultaneous carbonate dissolution (CD) and PP fuelled by NH_4^+, in equal proportion and would result in no

Table 1: Summary of the main net reactions occurring among the different zones of a redox gradient with reactants starting in equilibrium with the atmosphere, adapted from Soetaert et al. (2007). The calculations assume Redfield ratio of the organic matter, i. e. $\gamma N = 0.156$ and $\gamma P = 0.0094$ (Soetaert et al., 2007). Redox zones describe the different conditions required for completing the reaction.

Name	Redox zones	Net Formula	ΔTA	ΔDIC
AR	Oxic	$(CH2O)(NH3)_{\gamma N}(H3PO4)_{\gamma P} + O2 \rightarrow$ $\gamma^N NH3 + \gamma^P H3PO4 + CO2 + H2O$	0.15	+1
CD	Any	$CaCO_3 + CO_2 \rightarrow Ca^{2+} + 2\ HCO_3^-$	2	+1
NR-N2	Suboxic	$(CH_2O)(NH_3)_{\gamma N}(H_3PO_4)_{\gamma P} + 0.8\ HNO_3 \rightarrow$ $\gamma^N NH_3 + \gamma^P H_3PO_4 + CO_2 + 0.4\ N_2 + 1.4\ H_2O$	0.95	1
MnR-MnC	Suboxic	$(CH_2O)(NH_3)_{\gamma N}(H_3PO_4)_{\gamma P} + 2\ MnO_2 + CO_2 \rightarrow$ $\gamma^N NH_3 + \gamma^P H_3PO_4 + 2\ MnCO_3 + H_2O$	0.15	-1
SR	Sulfidic	$(CH_2O)(NH_3)_{\gamma N}(H_3PO_4)_{\gamma P} + 1/2\ H_2SO_4 \rightarrow$ $\gamma^N NH_3 + \gamma^P H_3PO_4 + CO_2 + 1/2\ H_2S + H_2O$	1.15	+1
SR-O	Sulfidic + Oxic	$(CH_2O)(NH_3)_{\gamma N}(H_3PO_4)_{\gamma P} + 1/2\ H_2SO_4 + O_2 \rightarrow$ $\gamma^N NH_3 + \gamma^P H_3PO_4 + CO_2 + 1/2\ H_2SO_4 + H_2O$	0.15	+1
SR-MnC	Sulfidic + Suboxic	$(CH_2O)(NH_3)_{\gamma N}(H_3PO_4)_{\gamma P} + 1/2\ H_2SO_4 + 0.5\ MnO_2 \rightarrow$ $\gamma^N NH_3 + \gamma^P H_3PO_4 + 1/2\ CO_2 + 1/2\ MnCO_3 + 0.5\ S^0 + 1.5\ H_2O$	1.15	+0.5
SR-FeS	Sulfidic + Suboxic	$(CH_2O)(NH_3)_{\gamma N}(H_3PO_4)_{\gamma P} + 0.44\ FeOOH + 0.44\ H_2SO_4 \rightarrow$ $\gamma^N NH_3 + \gamma^P H_3PO_4 + CO_2 + 0.44\ FeS + 1.67\ H_2O$	1.04	+1

DICex, only TAex production (see Table 2); the carbonate dissolution buffers the DIC consumption produced by PP. The Ca^{2+} concentrations observed by Su et al. (2021) and during the 2018 cruise (data not shown) vary linearly with salinity *i. e.* $[Ca^{2+}]$

$= 0.282$ S $+ 0.4$ in mmol L^{-1}. Assuming similar behaviour in 2017, calculations show that the whole water column is undersaturated with respect to calcite and validates the possibility for CD.

225   In 2018, below the PP zone down to $DICex = 240\mu M$, the beginning of the ILO zone, the TAex increases significantly with a $\Delta TAex/\Delta DICex$ signature incompatible with AR ($\Delta TAex/\Delta DICex = 0.67 \pm 0.1$, Fig. 3A) and a $\Delta DICex/\Delta AOU$ close to 1.5. Although there are other available candidates, a contribution of CD superimposed on AR seems most likely (theoretical $\Delta TAex/\Delta DICex$ slope of 2 for CD, Table 1). A linear combination fitting leads to TA contribution of 13% from AR and 87% from CD (Table 2) and results in $\Delta TAex/\Delta DICex = 0.77$ and $\Delta DICex/\Delta AOU = 1.5$. An explanation of its occurrence solely

230   in 2018 could be particularly carbonate rich suspended material at high flow conditions. Deeper, in the ILO zone, the relations of $\Delta TAex/\Delta DICex/\Delta AOU$ (Fig. 3) result from aerobic respiration with almost indiscernible carbonate precipitation ($\Delta TAex/\Delta DICex = 0.2$, $\Delta DICex/\Delta AOU = 0.8$). Overall, our results show that the higher river flow of 2018 increases carbonate

Table 2: Linear combination of reactions from Table 1 that fit the observations (see text for details, H_2O molecules are omitted).

		Linear combination	(for 1 CH_2O)	$\Delta TAex / \Delta DICex$	$\Delta DICex / \Delta AOU$ or $\Delta TAex / \Delta H2S$	Net Formula (for 1 mole of CH_2O)
Observed in 2017	Observed in 2018	Oxic	CD-AR	∞	-0	$\gamma^N NH_3 + \gamma^P H_3PO_4 + CaCO_3 + 2\ CO_2 + 2\ H_2O \rightarrow$ $(CH_2O)(NH_3)_{\gamma N}(H_3PO_4)_{\gamma P} + O_2 + Ca^{2+} + 2\ HCO_3^-$
			AR+0.5CD	0.77	1.5	$(CH_2O)(NH_3)_{\gamma N}(H_3PO_4)_{\gamma P} + O_2 + 0.5\ CaCO_3 \rightarrow$ $\gamma^N NH_3 + \gamma^P H_3PO_4 + 0.5\ CO_2 + 0.5\ Ca^{2+} + HCO_3^-$
			AR	0.15	1	$(CH_2O)(NH_3)_{\gamma N}(H_3PO_4)_{\gamma P} + O_2 \rightarrow$ $\gamma^N NH_3 + \gamma^P H_3PO_4 + CO_2$
		Suboxic	0.98 SR-MnC + 0.02 MnR-MnC	2.4		$(CH_2O)(NH_3)_{\gamma N}(H_3PO_4)_{\gamma P} + 0.49\ H_2SO_4 + 0.53\ MnO_2 \rightarrow$ $\gamma^N NH_3 + \gamma^P H_3PO_4 + 0.47\ CO_2 + 0.53\ MnCO_3 + 0.49\ S^0$
			0.65 SR-FeS + 0.35 MnR-MnC	2.4		$(CH_2O)(NH_3)_{\gamma N}(H_3PO_4)_{\gamma P} + 0.3\ H_2SO_4 + 0.7\ MnO_2 + 0.3\ FeOOH \rightarrow$ $\gamma^N NH_3 + \gamma^P H_3PO_4 + 0.3\ CO_2 + 0.7\ MnCO_3 + 0.29\ FeS$
			6.4 CD + MnR-MnC	2.4		$(CH_2O)(NH_3)_{\gamma N}(H_3PO_4)_{\gamma P} + 6.4\ CaCO_3 + 2\ MnO_2 + 7.4\ CO_2 \rightarrow$ $\gamma^N NH_3 + \gamma^P H_3PO_4 - 12.8\ HCO_3^- + 2\ MnCO_3 + 6.4\ Ca^{2+}$
		Sulfidic	0.38 MnR-MnC + 0.76 SR - 0.15 SR-MnC	2.4	2	$(CH_2O)(NH_3)_{\gamma N}(H_3PO_4)_{\gamma P} + 0.31\ H_2SO_4 + 0.68\ MnO_2 + 0.07\ S^0 \rightarrow$ $\gamma^N NH_3 + \gamma^P H_3PO_4 + 0.32\ CO_2 + 0.68\ MnCO_3 + 0.38\ H_2S$
			0.64 MnR-MnC + 1.36 SR - SR-MnC	2.4	0.75	$(CH_2O)(NH_3)_{\gamma N}(H_3PO_4)_{\gamma P} + 0.18\ H_2SO_4 + 0.79\ MnO_2 + 0.5\ S^0 \rightarrow$ $\gamma^N NH_3 + \gamma^P H_3PO_4 + 0.21\ CO_2 + 0.79\ MnCO_3 + 0.68\ H_2S$

dissolution for the top 5-10 m depth (at salinity below 8) that superimpose on primary production (for salinity below 4) or aerobic respiration (for salinity between 4 and 8).3.3. Sediment control

3.3.1 Identification of preponderant reactions

In the absence of oxygen, in the suboxic and sulfidic zone, both campaigns show a similar evolution of the TAex and DICex with very high ΔTAex/ΔDICex of 2.4 (Fig. 3a). This exceptionally high ratio, never reported in the literature, cannot be explained by most typical chemical reactions such carbonate dissolution (CD), aerobic respiration (AR), CO_2 uptake or primary production (PP = -AR). A scenario combining sulfate reduction (SR) is particularly attractive since SR represents the main carbon remineralisation pathway in absence of oxygen. However, a combination of SR with CD would result in a ΔTAex/ΔDICex between 1.15 and 2 (see Table 1 or Fig. 3c) and fails to reach the ΔTAex/ΔDICex of 2.4. Moreover, SR alone underestimates the importance of the H_2S oxidation pathway. H_2S oxidation is critical in the Chesapeake Bay since no H_2S is measurable in the suboxic zone while the gradient at the sediment/water interface indicates high H_2S sedimentary efflux (Fig. 1) and that oxidation can consume all the alkalinity produced during SR, as with oxygenated oxidation (see reaction SR-O in Table 1).

Generalizing these observations, recent efforts to build an alkalinity budget on the global scale (Hu and Cai, 2011; Middelburg et thal., 2020) highlight that the alkalinity produced by anaerobic respiration corresponds to the uncharged species produced, mostly in solid or gaseous phases. Indeed, the alkalinity changes produced during a natural reaction equal the "charges transfer" from species having some charge at pH = 4.5, such as NO_3^- and SO_4^{2-}, to "acid active species" that would lose its charges at pH = 4.5, mainly HCO_3^-, that does not count in the alkalinity calculation (see Eq. (4)). Although correct, this approach tends to neglect the roles of Fe and Mn oxides (Middelburg et al., 2020) since their transformation from (oxyhydr)oxides into sulphur or carbonate species does not involve any charge transfer. When looking in detail at these processes, the metal oxides are critical since they are the main H_2S oxidation pathway that does not regenerate H_2SO_4 but rather produces S^0 instead (Findlay et al., 2014; Avetisyan et al., 2021) which limits alkalinity consumption. The plot of selected redox sensitive species against TAex (Fig. 4) reveals a particular behaviour of MnOx in the suboxic water with a maximum concentration at the disappearance of O_2 followed by a decrease down to zero in presence of H_2S. Manganese changes from MnOx to Mn^{2+}, and ultimately to $MnCO_3$, consuming DIC and transforming H_2S to a non-charged species. This TA source is generally overlooked but may be important in the Chesapeake Bay. Fig. 2 and 4 also depict recycling of NO_2^- whose concentrations increase simultaneously to O_2. However, the small vertical shift between NO_2^- and O_2 minimum (Fig. 4) and the lack of overlap between NO_2^- and H_2S indicates that NO_2^- does not directly oxidize H_2S. Since, NH_4^+ and NO_3^- concentration were not measured, we limit our reasoning to the layer depleted in NO_2^-, that signals the negligible role of N cycling at these depths.
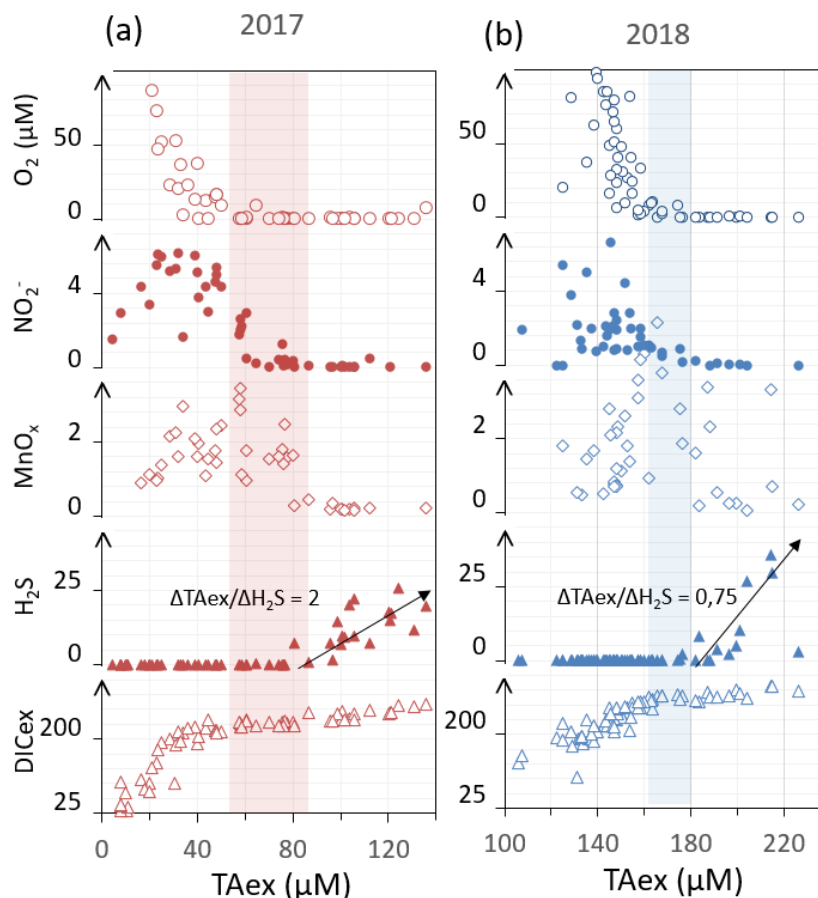
Figure 4: Evolution of selected species versus TAex for the 2017 (a) and 2018 (b) campaigns with the suboxic zone colored.

In the anoxic layer, most of the dissolved species are at too low concentration (*e.g.* Mn^{2+}_{aq}, Fe^{2+}_{aq}) to be a net reagent to affect the carbon cycle on a monthly time scale. These species are usually recycled rapidly and hold a role of catalyser or electron shuttle between other redox species. Therefore, to explain the 100 µM TAex increase in absence of oxygen (Fig. 3a), only aqueous species with "important" stock concentrations at a monthly timescale (with concentrations that frequently exceed 1 mM in anoxic porewater) are taken into account, *i. e.,* SO_4^{2-}, Ca^{2+}, H_2S, NH_4^+ together with gaseous (N_2, CO_2) and main solid phases (FeS, S^0, $MnCO_3$, $FeOOH$, MnO_2). Based on these species, we detailed the most likely preponderant reactions for each redox zone (Table 1), although, for the sake of simplicity, many mineral and associated reactions are neglected (*e.g.,* iron phosphate, ferrous or manganous oxide, sulphur clusters, adsorption processes, reverse weathering). For the suboxic zone, the nitrite reduction associated with N_2 production or denitrification (NR-N2, Table 1) and the manganese oxides reduction associated with manganese carbonates precipitation (MnR-MnC, Table 1) represent the main expected respiration processes. The reduction of HNO_3 down to NH_3 is not detailed but would result in almost similar alkalinity changes: 1.15 for NH_3 production (DNRA) versus 0.95 for N_2 production. The only solid form of Mn(II) is $MnCO_3$, since MnS is negligible despite

275 thermodynamic possibilities. $FeCO_3$ production would produce a very similar reaction as $MnCO_3$ production; the latter, more common, is favoured in this simple description. Accordingly, the only solid product from iron reactions is FeS and requires a coupling between iron oxide respiration and the minimum required amount of sulfate reduction (equation SR-FeS). However, FeS_2 is implicitly taken into account since it corresponds to FeS plus S_0 and a specific coupling of iron oxide respiration with sulfate reduction to produce FeS_2 would result in $\Delta TAex=1.21$ molC^{-1} instead of $\Delta TAex=1.04$ molC^{-1} when FeS is the final

280 product (Table 1). After sulfate reduction, H_2S can also accumulate in the water (SR reaction) or be oxidized back to SO_4^{2-} (SR-O is detailed as an example). Finally, SR-MnC describes H_2S oxidation by MnO_2 into S_0. Table 1 illustrates the importance of metal oxide to generate amount of high alkalinity in the case of sulfate reduction. In particular, it highlights that the higher $\Delta TAex/\Delta DICex$ obtained ratio is 2.3 which corresponds to a combination of sulfate reduction follow by Mn (or Fe) oxide reduction follow by Mn (or Fe) carbonate precipitation, and is here illustrated by the SR-MnC reaction from Table 1.

285 **3.3.2 Quantification of reactions importance**

In the absence of H_2S, the simplest combination leading to the observed $\Delta TAex/\Delta DICex$ of 2.4 ± 0.1 is to consider sulfide oxidation by MnOx and formation of $MnCO_3$ leading to the SR-MnC reaction (theoretical ratio of $\Delta TAex/\Delta DICex = 2.3$, see Table 1). More complex combinations to better fit the $\Delta TAex/\Delta DICex$ can be found graphically in Fig. 3d. Note here the arrows demonstrate that the slope of 2.4 can be obtained for any reaction in combination with MnR-MnC. Combinations

290 without MnR-MnC, however, leads to a negative SR and are not considered despite a possible small participation of anoxygenic phototrophic (purple) bacteria (Findlay et al., 2015, 2017). Therefore, in the absence of nitrate, oxygen and H_2S, only a combination of MnR-MnC with SR-MnC (producing S^0, Table 2), SR-FeS (producing FeS, Table 2) or CD (releasing Ca^{2+}, Table 2) gives the particularly high $\Delta TAex/\Delta DICex$ of 2.4. S_0 was not measured during our campaign, but it has been reported at this site (Findlay et al., 2014); thus, S_0 produced by SR-MnC can react with FeS to form FeS_2. The three identified

295 combinations require a critical role of MnO_2 in agreement with the observed remobilization in the hypoxic zone (Fig. 4). However, since the Ca^{2+} survey (Su et al. 2021) did not reveal a significant production in the Chesapeake Bay, and since the available data on iron speciation (Fig. 2) do not indicate any clear reaction, the combination of MnR-MnC with SR-MnC is most likely.

In the presence of H_2S, a closer look at the relation between ΔH_2S versus $\Delta TAex$ (Fig. 4) reveals an interannual variation

300 of the $\Delta TAex/\Delta H_2S$ ratio changing from 2 in 2017 to 0.75 in 2018 whereas the theoretical ratio of SR is $\Delta TAex/\Delta H_2S = 2.3$ when no H_2S is oxidized. These observed ratios indicates either TAex consumption without H_2S oxidation or H_2S formation without TAex production. The retained combination should implicate at least SR, to produce the H_2S, and MnR-MnC, to increase the $\Delta TAex/\Delta DICex$ slope, but it also requires another reaction to decrease the $\Delta TAex/\Delta H_2S$ ratio. Since carbonate under saturation prevents carbonate precipitation, and no primary production is expected, the most likely source of H_2S is from

305 S_0, although FeS_2 is also possible, as depicted in Table 2. From this equation, the main TA source is the absence of SO_4^{2-} regeneration after sulfate reduction whereas the second source is the nutrient release that accounts for 19% and 29% of the TA

produced in 2017 and 2018, respectively. The alternative possibility of NH_4^+ oxidation by MnO_2 into N_2 (Mn-anammox, (Luther et al., 1997; Thamdrup, 2012)) could also reduce the alkalinity without additional H_2S oxidation.

Based on the stoichiometry proposed, about 88 µM to 155 µM of MnO_2 are required to produce the 100 µM TAex increase observed (Fig. 3a), one order of magnitude higher than the observed MnOx concentration (Fig. 4). Based on an average concentration of 20 µmol g^{-1} of Mn in suspended particles, the 88 µM of MnO_2 would require a suspended material concentration of about 4.4 g L^{-1}, which is again one or two orders of magnitude higher than the 0.01 – 0.1 g L^{-1} usually found in the Chesapeake Bay. However, previous studies at this station (*e.g.,* Sholkovitz et al., 1992) explained the seasonality of anoxia with an upward move of the redox front from the sediments to bottom waters during the start of summer. Accordingly, it is likely that the observed dissolved species, notably TAex and DICex, have not been produced in the water column but rather in the sediment during the year and then transported simultaneously with other reduced elements as the summer begin. Therefore, the 100 µM TA increase does not fit with the ambient Mn^{2+} or MnO_2 in the water column but rather with the $MnCO_3$ deposited in the sediment. The sedimentary solid Mn stock is about 10 mM (assuming a porosity of 0.8, a solid density of 2.6 and a Mn content of 20 µmol g^{-1}), which largely exceeds the 88 µM required to produce the 100 µM TAex increase.

At a global scale, beside its role on alkalinity, MnO_2 can also be a trap for CO_2 as proposed in this Urey-Ebelman (Urey, 1952, Eq. 5) like reaction (Eq.6):

$$SiCaO_3 + CO_2 \rightarrow SiO_2 + CaCO_3 \qquad (5)$$

$$MnO_2 + CO_2 \rightarrow 0.5\ O_2 + MnCO_3 \qquad (6)$$

Assuming all the Mn is in the form of MnO_2, a weathering intensity similar to iron (Poulton and Raiswell, 2002) and based on the upper continental crust composition (Rudnick and Gao, 2003), the continental MnO_2 input to the ocean can be estimated at 0.4 x 10^{12} mol y^{-1}. Assuming a steady state ocean toward Mn and $MnCO_3$ as the unique sedimentary phase, this estimation represent 1.4 % of the total carbonate burial (Middelburg et al., 2020). Although negligible at the global scale, this carbonate burial may be significant in MnO_2 rich semi-enclosed basins.

Conclusion

The summer anoxia observed in the Chesapeake Bay is characterized by exceptional high $\Delta TAex/\Delta DICex$ of 2.4 which
330   has never been reported in anoxic water columns or sediment pore waters. By comparison, pore water $\Delta TAex/\Delta DICex$ was
measured at 1.15 in the Gulf of Mexico (Hu et al., 2010) with $\Delta TAex / \Delta H2S \sim 2.2$ as expected when sulfate reduction is
associated with H_2S accumulation (theoretical $\Delta TAex / \Delta H2S$ ratio from SR being 2.3, Table 1). In the Baltic Sea, a
$\Delta TAex/\Delta DICex$ ratio of 1.3 was reported (Lukawska-Matuszewska, 2016) with $\Delta TAex / \Delta H_2S > 17.5$, signs of important H_2S
consumption by Fe oxides. In oxygenated coastal sediment, where dissolved reduced compounds are oxidised before release
335   in the water columns, fluxes of TA over fluxes of DIC ranged from 0.4 to 1 (Rassmann et al., 2020 and references therein). In
the Chesapeake Bay, $\Delta TAex / \Delta H_2S$ is below 2.3, a sign of another preponderant reaction. The stoichiometry analysis agrees
with direct measurements to underline the critical role of MnO_2 reduction followed by Mn carbonate precipitation. This
scenario could be confirmed by a careful analysis of Mn oxides concentration in the bottom sediment during the entire year,
since semi-enclosed basins are known to concentrate manganese oxides into the deeper area during oxygenated conditions
340   (Thamdrup and Dalsgaard, 2000; Madison et al., 2013; Lenstra et al., 2020). Despite the fact that $MnCO_3$ production from
MnO_2 involves no charge transfer (Hu and Cai, 2011), our study demonstrates that it can have strong impact on local alkalinity
(Middelburg et al., 2020). The lack of charge transfer visible from the stoichiometry implies that Mn has no bearing on the
alkalinity it produces, but it is a critical element to limit the H_2S oxidation to its S_0 intermediate form and finally to favour its
burial.

345   **Appendix A**
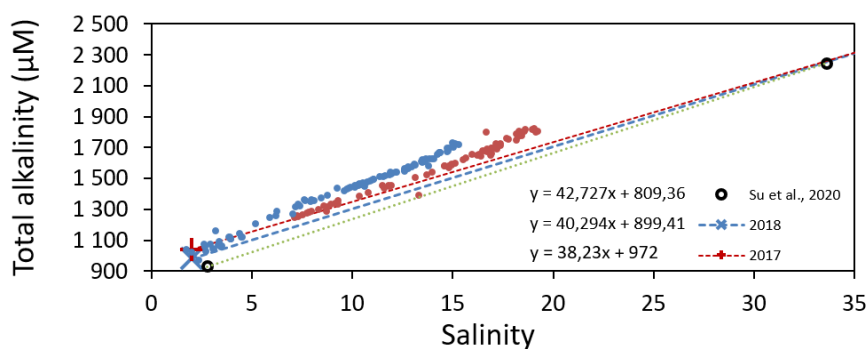
Figure A1: Variation of Total Alkalinity (TA) during oceanic and river mixing. Dashed lines represent the theoretical TA if only mixing occurs (TAex=0).
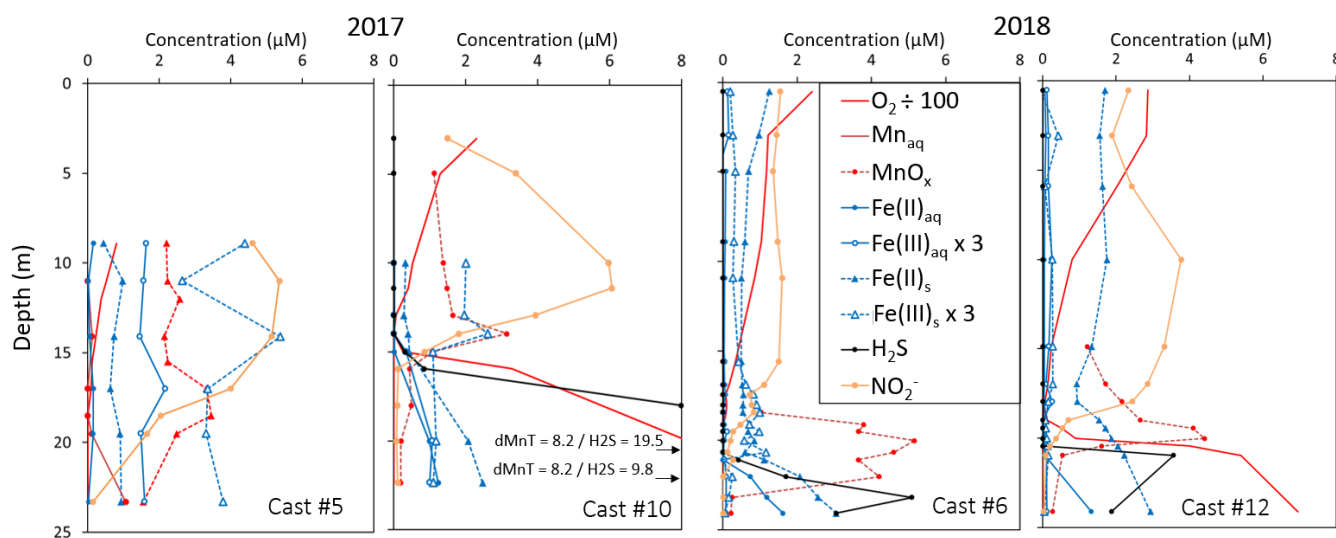
Figure A2: Examples of redox and metal chemistry profiles. Note that Fe(III)$_s$ and Fe(III)$_{aq}$ scales are zoomed in by 3 and O$_2$ scale is zoomed out by 100.

Data availability

The data used in this paper is available on request to the correspond author.

350 *Author contribution*

ATC, ERE, JN, BMT and SJ performed the data analysis. ATC and SJ process the data. ATC, GWL, SJ and WJC interpreted the results. GWL, BMT and WJC get the funding. ATC wrote the paper with contributions from all authors.

Competing interests

The authors declare that they have no conflict of interest.

355 *Acknowledgements*

We gratefully acknowledge the support of the captain and crew of *R/V Hugh R. Sharp*. This work was funded by grants from the Chemical Oceanography program of the National Science Foundation (OCE-1558738 to GWL; OCE-1558692 to BMT and OCE-1756815 to WJC)

References

360 Abril, G., Etcheber, H., Delille, B., Frankignoulle, M., and Borges, A. V.: Carbonate dissolution in the turbid and eutrophic Loire estuary, Mar. Ecol. Prog. Ser., 259, 129–138, 2003.

Alshameri, A., He, H., Zhu, J., Xi, Y., Zhu, R., Ma, L., and Tao, Q.: Adsorption of ammonium by different natural clay minerals: Characterization, kinetics and adsorption isotherms, Appl. Clay Sci., 159, 83–93, https://doi.org/10.1016/j.clay.2017.11.007, 2018.

365 Avetisyan, K., Zweig, I., Luther, G. W., and Kamyshny, A.: Kinetics and mechanism of polysulfides and elemental sulfur formation by a reaction between hydrogen sulfide and δ-MnO2, Geochim. Cosmochim. Acta, 313, 21–37, https://doi.org/10.1016/j.gca.2021.08.022, 2021.

Borges, A. V., Schiettecatte, L.-S., Abril, G., Delille, B., and Gazeau, F.: Carbon dioxide in European coastal waters, Estuar. Coast. Shelf Sci., 70, 375–387, https://doi.org/10.1016/j.ecss.2006.05.046, 2006.

370 Borges, A. V., Abril, G., and Bouillon, S.: Carbon dynamics and CO2 and CH4 outgassing in the Mekong delta, Biogeosciences, 15, 1093–1114, https://doi.org/10.5194/bg-15-1093-2018, 2018.

Boudreau, B. P., Middelburg, J. J., and Luo, Y.: The role of calcification in carbonate compensation, Nat. Geosci., 11, 894–900, https://doi.org/10.1038/s41561-018-0259-5, 2018.

Cai, W.-J., Huang, W.-J., Luther, G. W., Pierrot, D., Li, M., Testa, J., Xue, M., Joesoef, A., Mann, R., Brodeur, J., Xu, Y.-Y., Chen, B., Hussain, N., Waldbusser, G. G., Cornwell, J., and Kemp, W. M.: Redox reactions and weak buffering capacity lead to acidification in the Chesapeake Bay, Nat. Commun., 8, 369, https://doi.org/10.1038/s41467-017-00417-7, 2017.

Chen, B., Cai, W.-J., Brodeur, J. R., Hussain, N., Testa, J. M., Ni, W., and Li, Q.: Seasonal and spatial variability in surface pCO2 and air–water CO2 flux in the Chesapeake Bay, Limnol. Oceanogr., 65, 3046–3065, https://doi.org/10.1002/lno.11573, 2020.

Clement, B. G., Luther, G. W., and Tebo, B. M.: Rapid, oxygen-dependent microbial Mn(II) oxidation kinetics at sub-micromolar oxygen concentrations in the Black Sea suboxic zone, Geochim. Cosmochim. Acta, 73, 1878–1889, https://doi.org/10.1016/j.gca.2008.12.023, 2009.

Cotovicz Jr., L. C., Libardoni, B. G., Brandini, N., Knoppers, B. A., and Abril, G.: Comparisons between real-Time PCO2 measurements with indirect estimates in two contrasting Brazilian estuaries: The eutrophic guanabara bay (RJ) and the oligotrophic sao francisco River estuary (AL), Quím. Nova, 39, 1206–1214, https://doi.org/10.21577/0100-4042.20160145, 2016.

Dickson, A. G.: An exact definition of total alkalinity and a procedure for the estimation of alkalinity and total inorganic carbon from titration data, Deep Sea Res. Part Oceanogr. Res. Pap., 28, 609–623, https://doi.org/10.1016/0198-0149(81)90121-7, 1981.

Findlay, A. J., Gartman, A., MacDonald, D. J., Hanson, T. E., Shaw, T. J., and Luther, G. W.: Distribution and size fractionation of elemental sulfur in aqueous environments: The Chesapeake Bay and Mid-Atlantic Ridge, Geochim. Cosmochim. Acta, 142, 334–348, 2014.

Findlay, A. J., Bennett, A. J., Hanson, T. E., and Luther, G. W.: Light-Dependent Sulfide Oxidation in the Anoxic Zone of the Chesapeake Bay Can Be Explained by Small Populations of Phototrophic Bacteria, Appl. Environ. Microbiol., 81, 7560–7569, https://doi.org/10.1128/AEM.02062-15, 2015.

Findlay, A. J., Di Toro, D. M., and Luther, G. W.: A model of phototrophic sulfide oxidation in a stratified estuary, Limnol. Oceanogr., 62, 1853–1867, https://doi.org/10.1002/lno.10539, 2017.

Friedlingstein, P., Jones, M. W., O'Sullivan, M., Andrew, R. M., Hauck, J., Peters, G. P., Peters, W., Pongratz, J., Sitch, S., Le Quéré, C., Bakker, D. C. E., Canadell, J. G., Ciais, P., Jackson, R. B., Anthoni, P., Barbero, L., Bastos, A., Bastrikov, V., Becker, M., Bopp, L., Buitenhuis, E., Chandra, N., Chevallier, F., Chini, L. P., Currie, K. I., Feely, R. A., Gehlen, M., Gilfillan, D., Gkritzalis, T., Goll, D. S., Gruber, N., Gutekunst, S., Harris, I., Haverd, V., Houghton, R. A., Hurtt, G., Ilyina, T., Jain, A. K., Joetzjer, E., Kaplan, J. O., Kato, E., Klein Goldewijk, K., Korsbakken, J. I., Landschützer, P., Lauvset, S. K., Lefèvre, N., Lenton, A., Lienert, S., Lombardozzi, D., Marland, G., McGuire, P. C., Melton, J. R., Metzl, N., Munro, D. R., Nabel, J. E. M. S., Nakaoka, S.-I., Neill, C., Omar, A. M., Ono, T., Peregon, A., Pierrot, D., Poulter, B., Rehder, G., Resplandy, L., Robertson, E., Rödenbeck, C., Séférian, R., Schwinger, J., Smith, N., Tans, P. P., Tian, H., Tilbrook, B., Tubiello, F. N., van der Werf, G. R., Wiltshire, A. J., and

Zaehle, S.: Global Carbon Budget 2019, Earth Syst. Sci. Data, 11, 1783–1838,
410   https://doi.org/10.5194/essd-11-1783-2019, 2019.

Grasshoff, K.: Determination of nitrite, nitrate, oxygen, thiosulphate, in: Methods of seawater analysis,
New York, 61–72, 1983.

Heiss, E. M. and Fulweiler, R. W.: Coastal water column ammonium and nitrite oxidation are decoupled
in summer, Estuar. Coast. Shelf Sci., 178, 110–119, https://doi.org/10.1016/j.ecss.2016.06.002, 2016.

415   Horrigan, S. G., Montoya, J. P., Nevins, J. L., McCarthy, J. J., Ducklow, H., Goericke, R., and Malone,
T.: Nitrogenous nutrient transformations in the spring and fall in the Chesapeake Bay, Estuar. Coast. Shelf
Sci., 30, 369–391, https://doi.org/10.1016/0272-7714(90)90004-B, 1990.

Hu, X. and Cai, W.-J.: An assessment of ocean margin anaerobic processes on oceanic alkalinity budget,
Glob. Biogeochem. Cycles, 25, https://doi.org/10.1029/2010GB003859, 2011.

420   Hu, X., Cai, W.-J., Wang, Y., Luo, S., and Guo, X.: Pore-water geochemistry of two contrasting brine-
charged seep sites in the northern Gulf of Mexico continental slope, Mar. Chem., 118, 99–107,
https://doi.org/10.1016/j.marchem.2009.11.006, 2010.

Hudson, J. M., MacDonald, D. J., Estes, E. R., and Luther, G. W.: A durable and inexpensive pump
profiler to monitor stratified water columns with high vertical resolution, Talanta, 199, 415–424,
425   https://doi.org/10.1016/j.talanta.2019.02.076, 2019.

Ishii, H., Koh, H., and Satoh, K.: Spectrophotometric determination of manganese utilizing metal ion
substitution in the cadmium-α, β,-γ, δ-tetrakis (4-carboxyphenyl) porphine complex, Anal. Chim. Acta,
136, 347–352, 1982.

Joesoef, A., Kirchman, D. L., Sommerfield, C. K., and Cai, W.-J.: Seasonal variability of the inorganic
430   carbon system in a large coastal plain estuary, Biogeosciences, 14, 4949–4963,
https://doi.org/10.5194/bg-14-4949-2017, 2017.

Jones, M. R., Luther, G. W., Mucci, A., and Tebo, B. M.: Concentrations of reactive Mn(III)-L and MnO2
in estuarine and marine waters determined using spectrophotometry and the leuco base, leucoberbelin
blue, Talanta, 200, 91–99, https://doi.org/10.1016/j.talanta.2019.03.026, 2019.

435   Lenstra, W. K., Séguret, M. J. M., Behrends, T., Groeneveld, R. K., Hermans, M., Witbaard, R., and
Slomp, C. P.: Controls on the shuttling of manganese over the northwestern Black Sea shelf and its fate
in   the   euxinic   deep   basin,   Geochim.   Cosmochim.   Acta,   273,   177–204,
https://doi.org/10.1016/j.gca.2020.01.031, 2020.

Lewis, B. L., Glazer, B. T., Montbriand, P. J., Luther, G. W., Nuzzio, D. B., Deering, T., Ma, S., and
440   Theberge, S.: Short-term and interannual variability of redox-sensitive chemical parameters in

hypoxic/anoxic bottom waters of the Chesapeake Bay, Mar. Chem., 105, 296–308, https://doi.org/10.1016/j.marchem.2007.03.001, 2007.

Lohrenz, S. E., Cai, W.-J., Chen, F., Chen, X., and Tuel, M.: Seasonal variability in air-sea fluxes of CO 2 in a river-influenced coastal margin, J. Geophys. Res., 115, 2010.

445 Lukawska-Matuszewska, K.: Contribution of non-carbonate inorganic and organic alkalinity to total measured alkalinity in pore waters in marine sediments (Gulf of Gdansk, S-E Baltic Sea), Mar. Chem., 186, 211–220, https://doi.org/10.1016/j.marchem.2016.10.002, 2016.

Luther, G. W.: The role of one-and two-electron transfer reactions in forming thermodynamically unstable intermediates as barriers in multi-electron redox reactions, Aquat. Geochem., 16, 395–420, 2010.

450 Luther, G. W., Sundby, B., Lewis, B. L., Brendel, P. J., and Silverberg, N.: Interactions of manganese with the nitrogen cycle: alternative pathways to dinitrogen, Geochim. Cosmochim. Acta, 61, 4043–4052, 1997.

Madison, A. S., Tebo, B. M., and Luther, G. W.: Simultaneous determination of soluble manganese(III), manganese(II) and total manganese in natural (pore)waters, Talanta, 84, 374–381, 455 https://doi.org/10.1016/j.talanta.2011.01.025, 2011.

Madison, A. S., Tebo, B. M., Mucci, A., Sundby, B., and Luther, G. W.: Abundant porewater Mn (III) is a major component of the sedimentary redox system, science, 341, 875–878, 2013.

Meybeck, M.: Global chemical weathering of surficial rocks estimated from river dissolved loads, Am. J. Sci., 287, 401–428, 1987.

460 Meybeck, M.: Global occurrence of major elements in rivers, Treatise Geochem., 5, 605, 2003.

Meybeck, M., Cauwet, G., Dessery, S., Somville, M., Gouleau, D., and Billen, G.: Nutrients (organic C, P, N, Si) in the eutrophic River Loire (France) and its estuary, Estuar. Coast. Shelf Sci., 27, 595–624, https://doi.org/10.1016/0272-7714(88)90071-6, 1988.

Middelburg, J. J., Soetaert, K., and Hagens, M.: Ocean Alkalinity, Buffering and Biogeochemical 465 Processes, Rev. Geophys., 58, e2019RG000681, https://doi.org/10.1029/2019RG000681, 2020.

Millero, F. J.: Thermodynamics of the carbon dioxide system in the oceans, Geochim. Cosmochim. Acta, 59, 661–677, https://doi.org/10.1016/0016-7037(94)00354-O, 1995.

Oldham, V. E., Jones, M. R., Tebo, B. M., and Luther, G. W.: Oxidative and reductive processes contributing to manganese cycling at oxic-anoxic interfaces, Mar. Chem., 195, 122–128, 470 https://doi.org/10.1016/j.marchem.2017.06.002, 2017a.

Oldham, V. E., Miller, M. T., Jensen, L. T., and Luther, G. W.: Revisiting Mn and Fe removal in humic rich estuaries, Geochim. Cosmochim. Acta, 209, 267–283, https://doi.org/10.1016/j.gca.2017.04.001, 2017b.

Poulton, S. W. and Raiswell, R.: The low-temperature geochemical cycle of iron: from continental fluxes
475   to marine sediment deposition, Am. J. Sci., 302, 774–805, 2002.

Raaphorst, W. V. and Malschaert, J. F. P.: Ammonium adsorption in superficial North Sea sediments, Cont. Shelf Res., 16, 1415–1435, https://doi.org/10.1016/0278-4343(95)00081-X, 1996.

Rassmann, J., Eitel, E. M., Lansard, B., Cathalot, C., Brandily, C., Taillefert, M., and Rabouille, C.: Benthic alkalinity and dissolved inorganic carbon fluxes in the Rhône River prodelta generated by
480   decoupled aerobic and anaerobic processes, Biogeosciences, 17, 13–33, https://doi.org/10.5194/bg-17-13-2020, 2020.

Raven, J. A., Wollenweber, B., and Handley, L. L.: A comparison of ammonium and nitrate as nitrogen sources for photolithotrophs, New Phytol., 121, 19–32, https://doi.org/10.1111/j.1469-8137.1992.tb01088.x, 1992.

485   Rickard, D. and Luther, G. W.: Chemistry of Iron Sulfides, Chem. Rev., 107, 514–562, https://doi.org/10.1021/cr0503658, 2007.

Rudnick, R. L. and Gao, S.: Composition of the continental crust, Treatise Geochem., 3, 1–64, 2003.

Shen, C., Testa, J. M., Li, M., Cai, W.-J., Waldbusser, G. G., Ni, W., Kemp, W. M., Cornwell, J., Chen, B., Brodeur, J., and Su, J.: Controls on Carbonate System Dynamics in a Coastal Plain Estuary: A
490   Modeling Study, J. Geophys. Res. Biogeosciences, 124, 61–78, https://doi.org/10.1029/2018JG004802, 2019.

Sholkovitz, E. R., Shaw, T. J., and Schneider, D. L.: The geochemistry of rare earth elements in the seasonally anoxic water column and porewaters of Chesapeake Bay, Geochim. Cosmochim. Acta, 56, 3389–3402, 1992.

495   Smith, S. V. and Mackenzie, F. T.: The Role of CaCO3 Reactions in the Contemporary Oceanic CO2 Cycle, Aquat. Geochem., 22, 153–175, https://doi.org/10.1007/s10498-015-9282-y, 2016.

Soetaert, K., Hofmann, A. F., Middelburg, J. J., Meysman, F. J. R., and Greenwood, J.: The effect of biogeochemical processes on pH, Mar. Chem., 105, 30–51, https://doi.org/10.1016/j.marchem.2006.12.012, 2007.

500   Stookey, L. L.: Ferrozine—a new spectrophotometric reagent for iron, Anal. Chem., 42, 779–781, 1970.

Su, J., Cai, W.-J., Brodeur, J., Chen, B., Hussain, N., Yao, Y., Ni, C., Testa, J. M., Li, M., Xie, X., Ni, W., Scaboo, K. M., Xu, Y., Cornwell, J., Gurbisz, C., Owens, M. S., Waldbusser, G. G., Dai, M., and Kemp, W. M.: Chesapeake Bay acidification buffered by spatially decoupled carbonate mineral cycling, Nat. Geosci., 13, 441–447, https://doi.org/10.1038/s41561-020-0584-3, 2020a.

505 Su, J., Cai, W., Brodeur, J., Hussain, N., Chen, B., Testa, J. M., Scaboo, K. M., Jaisi, D. P., Li, Q., Dai, M., and Cornwell, J.: Source partitioning of oxygen-consuming organic matter in the hypoxic zone of the Chesapeake Bay, Limnol. Oceanogr., 65, 1801–1817, https://doi.org/10.1002/lno.11419, 2020b.

Su, J., Cai, W., Testa, J. M., Brodeur, J. R., Chen, B., Scaboo, K. M., Li, M., Shen, C., Dolan, M., Xu, Y., Zhang, Y., and Hussain, N.: Supply-controlled calcium carbonate dissolution decouples the seasonal 510 dissolved oxygen and pH minima in Chesapeake Bay, Limnol. Oceanogr., lno.11919, https://doi.org/10.1002/lno.11919, 2021.

Thamdrup, B.: New Pathways and Processes in the Global Nitrogen Cycle, Annu. Rev. Ecol. Evol. Syst., 43, 407–428, https://doi.org/10.1146/annurev-ecolsys-102710-145048, 2012.

Thamdrup, B. and Dalsgaard, T.: The fate of ammonium in anoxic manganese oxide-rich marine 515 sediment, Geochim. Cosmochim. Acta, 64, 4157–4164, https://doi.org/10.1016/S0016-7037(00)00496-8, 2000.

Thibault de Chanvalon, A. and Luther, G. W.: Mn speciation at nanomolar concentrations with a porphyrin competitive ligand and UV–vis measurements, Talanta, 200, 15–21, https://doi.org/10.1016/j.talanta.2019.02.069, 2019.

520 Trouwborst, R. E., Clement, B. G., Tebo, B. M., Glazer, B. T., and Luther, G. W.: Soluble Mn(III) in Suboxic Zones, Science, 313, 1955–1957, https://doi.org/10.1126/science.1132876, 2006.

Urey, H. C.: On the Early Chemical History of the Earth and the Origin of Life, Proc. Natl. Acad. Sci., 38, 351–363, https://doi.org/10.1073/pnas.38.4.351, 1952.

Wolf-Gladrow, D. A., Zeebe, R. E., Klaas, C., Körtzinger, A., and Dickson, A. G.: Total alkalinity: The 525 explicit conservative expression and its application to biogeochemical processes, Mar. Chem., 106, 287–300, https://doi.org/10.1016/j.marchem.2007.01.006, 2007.

Zeebe, R. E. and Wolf-Gladrow, D.: CO2 in seawater: equilibrium, kinetics, isotopes, Gulf Professional Publishing, 2001.

Zhang, Q., Brady, D. C., Boynton, W. R., and Ball, W. P.: Long-Term Trends of Nutrients and Sediment 530 from the Nontidal Chesapeake Watershed: An Assessment of Progress by River and Season, JAWRA J. Am. Water Resour. Assoc., 51, 1534–1555, https://doi.org/10.1111/1752-1688.12327, 2015.